www.springer.com/41230
https://doi.org/10.1007/s41230-025-5007-z
Research & Development
Vol. 22 No. 2 March 2025
CHINA FOUNDRY

# Kelvin lattice structures fabricated by laser powder bed fusion: Design, preparation, and mechanical performance

**Yan-peng Wei[1, 2], Huai-qian Li[1], Ying-chun Ma[1], Zhi-quan Miao[1], *Bo Yu[1], and **Feng Lin[2]**

*1. State Key Laboratory of Advanced Casting Technologies, Shenyang Research Institute of Foundry Co., Ltd. CAM, Shenyang 110022, China*

*2. Department of Mechanical Engineering, Tsinghua University, Beijing 100084, China*



**Abstract:** Metallic lattice structures represent advanced architected materials delivering exceptional properties with promising lightweight potential. With the rapid advancement of additive manufacturing, these structures have garnered increasing research interest. However, most metallic lattice structures generally exhibit anisotropic characteristics, which limits their application ranges. Additionally, a limited number of studies have successfully developed precise mechanical models, which have undergone experimental validation, for the purpose of describing the mechanical response exhibited by additively manufactured metallic lattice structures. In this study, Kelvin lattice structures with varying porosities were systematically designed and fabricated using laser powder bed fusion (LPBF) technology. By integrating finite element simulations with experimental characterization, an enhanced mechanical model was developed through a modification of the Gibson-Ashby model, providing an accurate quantitative description of the relationship between porosity and mechanical properties. The results show that the revised mechanical model can accurately describe the relationship between the geometric parameters and properties of metallic lattice structures. Specifically, the designed Kelvin lattice structures exhibit a smooth stress-strain curve with an obvious yield platform, demonstrating isotropic mechanical properties in all the three spatial directions. This enhances their suitability for complex loading conditions. Meanwhile, the microstructure and manufacturing accuracy of the Kelvin lattice structures were observed and analyzed by micro computed tomography. The results show that the fabricated metallic lattice structures achieved precise dimensional control and optimal densification. This study presents the complete process involved in modeling the Kelvin structure, including its conceptualization, manufacturing, implementation, and ultimately, disposal.

**Keywords:** Kelvin structure; metallic lattice structures; laser powder bed fusion; mechanical model; isotropic mechanical properties

**CLC numbers:** TG146.1+5 **Document code:** A **Article ID:** 1672-6421(2025)02-117-11

## 1 Introduction

Metallic lattice structures, as a kind of porous structures, possess the structural characteristics of lightweight, high specific strength and stiffness, as well as functional characteristics of reducing vibration and noise, and remarkable capacity for energy absorption [1-4]. Kelvin structures have garnered significant attention from the international academic community due to their promising potential as lightweight materials. They are widely used in aerospace, shipbuilding industries, among other fields, and have broad application prospects [5].

The conventional methods for preparing metallic lattice structures mainly include investment casting [6], stamping forming, and metal wire weaving [7]. Investment casting can fabricate metallic lattice structures with complex pore structures, but the preparation process is long and complex. Meanwhile, due to the limitation of the casting process, the metallic lattice structures fabricated by investment casting tend to have a

***Bo Yu**

Male, born in 1963, Ph. D., Research Fellow. His research interests mainly focus on the development of advanced functional materials, design and fabrication of porous metals, and directional solidification process for superalloy turbine blade.

E-mail: yub@chinasrif.com

****Feng Lin**

E-mail: linfeng@tsinghua.edu.cn

**Received: 2025-01-14; Revised: 2025-02-07; Accepted: 2025-03-17**

relatively large diameter. This makes it challenging to prepare metallic lattice structures with fine structures [8-9]. Among them, both the stamping forming method and the wire weaving method require higher ductility of the matrix materials, which restricts the range of materials that can be selected for these processes. Additionally, the hole structure that can be achieved using these methods is relatively simple [10].

Additive manufacturing technology has enabled the transition from process-constrained design to function-driven design, thereby enabling the integration of structure and function throughout the design and fabrication process [9,11-17]. Among the various additive manufacturing methods, the laser powder bed fusion (LPBF) technique stands out for its utilization of the layer-by-layer deposition principle in fabricating intricate structures [18-19]. This method offers remarkable processing accuracy and simplicity [20], particularly excelling in the production of metallic lattice structures characterized by small struts and elaborate pore architectures [21]. As a result, LPBF has become widely adopted in the aerospace industry for manufacturing components from materials such as nickel-based superalloys, steels, and titanium alloys [22-23]. However, the porous structure of metallic lattice structures prepared by LPBF is generally limited to simple cubic, pyramid, and Kagome structure, etc [24-25]. Existing studies indicate that the mechanical properties of these structures are often highly anisotropic, which severely restricts the adaptability of metallic lattice structures to complex working conditions and hinders their widespread application in aerospace, shipbuilding, and other fields [27-28].

The persuit for metallic lattice structures with isotropic properties has long been a primary goal for researchers. The initial study of the Kelvin structure originated from observations of the bubbles in liquids, as shown in Fig. 1(a). These bubbles undergo a process of formation, growth, merging, and rupture. During bubble merging, its shape evolves from a circular structure to a more complex polyhedral structure. Plateau's hypothesis, proposed in 1873, suggested that bubbles follow the principle of the minimum surface area of the liquid film during this process, and this hypothesis has been continuously validated in subsequent studies [29]. In 1887, Kelvin introduced the concept of a perfect foam structure based on the Plateau hypothesis [30]: The foam structure should be a three-dimensional polyhedral structure composed of 14 faces, consisting of 8 hexahedrons and 6 tetrahedrons [Fig. 1(b)]. In honor of Kelvin, this tetradecahedron structure is named the Kelvin structure. At present, various design schemes based on the Kelvin structure are applied in famous architectural structures, such as the Beijing Water Cube in Fig. 1(c), building block toys in Fig. 1(d), showing its broad applicability across different technical fields. In this study, the strut-based Kelvin unit was introduced into the design of metallic lattice structures, and its potential for improvement of mechanical properties was explored.

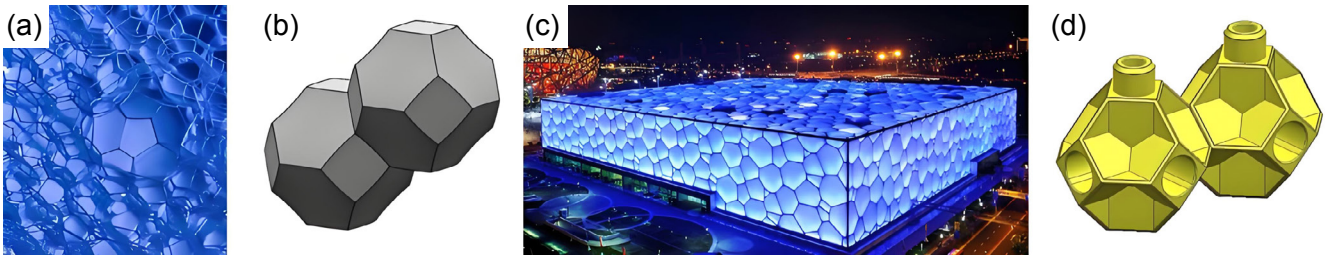


**Fig. 1: Bubbles in the liquid (a), Kelvin structure (b), Beijing Water Cube (c), building block toys (d) [29-30]**

Beyond the manufacturing process, it is essential to predict the mechanical properties and establish an appropriate model to provide the theoretical foundation for the manufacturing process [31]. The classical Gibson and Ashby model is frequently used to predict the mechanical properties of metallic lattice structures. When using LPBF technology to fabricate metallic lattice structures, this model can accurately describe the mechanical properties [20,32]. However, due to the variability of the Gibson and Ashby coefficients, the model manifests in multiple forms, resulting in a wide range of predicted values. Furthermore, the model only considers porosity of the porous structure, neglecting the effect of the shape factor on predictions. Additionally, many of these models are limited to theoretical derivations and lack experimental validation.

IN718 is an age-hardening nickel-based superalloy, known for its outstanding balance of mechanical properties, weldability, and manufacturability, especially its high-temperature strength, which reaches approximately 700 °C, and its good corrosion resistance [33]. Therefore, this study used IN718 as the matrix material for the lattice structure.

In this study, IN718 Kelvin lattice structures were designed and fabricated using LPBF, overcoming the limitations of previous research, which included a narrow selection of materials and a focus on single hole structures. This approach enabled the creation of metallic lattice structures with a broader range of possibilities. The manufacturing accuracy of the fabricated metallic lattice structures was characterized by scanning electron microscopy and micro-CT technology. By combining finite element analysis with experimental validation, the Gibson and Ashby model was modified, enabling more accurate predictions of mechanical properties. Moreover, this work addressed the anisotropic mechanical properties of metallic lattice structures in earlier studies and achieved isotropic mechanical properties in these structures.

# 2 Experimental methodology

## 2.1 Design and manufacturing

The basic parameters that determine the Kelvin structure are the strut length $L$ and the strut diameter $d$. Once these two parameters are specified, the Kelvin lattice structure is fully defined. Other parameters of the Kelvin structure include the minimum pore diameter $R_0$, the intermediate pore diameter $R_1$, and the unit cell pore diameter $R_2$. The Kelvin unit structure is shown in Fig. 2.

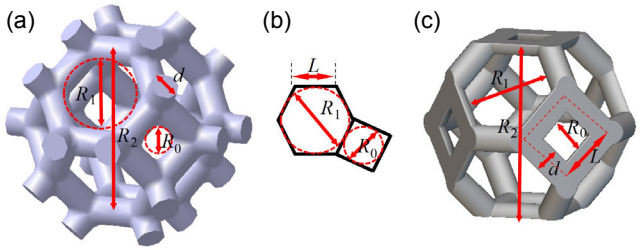


**Fig. 2: (a) Basic Kelvin structure; (b) relationship between $L$ and $R_1$ and $R_0$; (c) pretreated Kelvin structure**

The relationship between the geometric parameters of the Kelvin unit structure is as follows:

$$R_0 = L - d \quad (1)$$

$$R_1 = \sqrt{3}L - d \quad (2)$$

$$R_2 = 2\sqrt{2}L \quad (3)$$

The porosity of the metallic lattice structures can be calculated by dividing the pore volume of the lattice by the total cubic volume. The porosity is a design parameter, which is determined prior to fabrication. According to the above relationship, for a Kelvin unit structure with a specific pore type, metallic lattice structures with different porosities can be designed by adjusting the two parameters, $L$ and $d$. Therefore, by considering the strut length $L$ and the strut diameter $d$ as independent variables, lattice unit structures with varying pore sizes and porosities can be designed. These structures can then be expanded in three spatial dimensions, enabling the design of various series of three-dimensional metallic lattice structure models. Figure 3 shows the lattice structures with different porosities achieved by adjusting the $L/d$ ratios. As the value of $L/d$ increases, the porosity also increases.

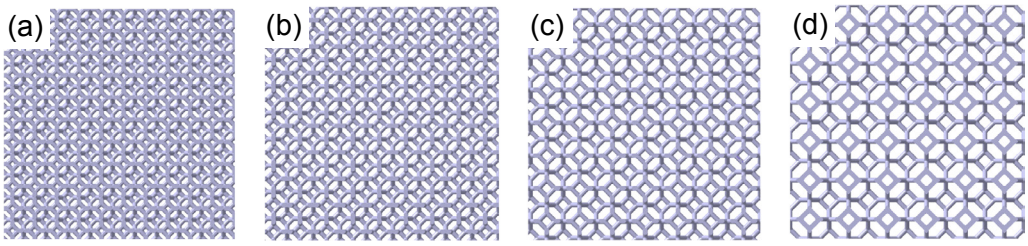


**Fig. 3: Kelvin lattice structure with different porosities: (a) 71%; (b) 82%; (c) 88%; (d) 92%**

Samples were prepared using a LPBF machine (BLT-310, China) under an argon inert gas atmosphere, with the laser power of 200 W, the scanning speed of 900 mm·s$^{-1}$, the scanning distance of 0.10 mm, and the powder layer thickness of 40 μm. The composition of the powder, with a particle size of 13–53 μm, is detailed in Table 1.

**Table 1: Chemical composition of IN718 powder (wt.%)**

| Ni | Cr | Mo | C | Nb | Al | Ti | Fe |
|---|---|---|---|---|---|---|---|
| 52.6 | 19.7 | 3.0 | 0.024 | 5.1 | 0.6 | 1.1 | Bal. |

## 2.2 Characterization and testing

Scanning electron microscopy (SEM, Sigma300, Zeiss, Germany) was used to investigate the surface morphology of the metallic lattice structures as well as the satellite powder particles adhered to the lattice surface. Nondestructive testing was performed using micro-CT (Granpect Company Limited, China) to evaluate printing accuracy and assess the quality of the additive manufacturing process. The mechanical properties of both the matrix material and metallic lattice structures were tested using a universal testing machine (DDL300, China), with a tensile speed of 1 mm·min$^{-1}$ until failure of the matrix sample, and the compression tests were carried out at a compression speed of 1 mm·min$^{-1}$. The test was terminated upon reaching either a recorded force of 300 kN or the onset of densification, at which point the load-displacement curve was obtained.

## 2.3 Finite element analysis

Finite element analyses were performed using ANSYS software. The equivalent elastic modulus and yield strength of metallic lattice structures with different porosities were obtained through finite element numerical simulation of quasi-static compression. The finite element software was employed to perform quasi-static compression on the designed metallic lattice structures. The relationship between porosity, elastic modulus, and yield strength was established through the stress-strain curve. The loading model for the quasi-static compression simulation is shown in Fig. 4(a). In the simulation, the lower plate was set as the fixed boundary condition, and the upper plate was set as the displacement boundary condition. Figure 4(b) shows the meshing of the quasi-static compression model. Each compression volume was divided into 1 million to 2 million elements to ensure accurate compression simulation.The overall compressive strain was maintained above 20% to ensure that the equivalent elastic modulus and yield strength could be derived from the simulation results. The matrix material was set as IN718 superalloy. The mechanical properties of the IN718 superalloy were determined through tensile tests, and the basic mechanical model of the IN718 superalloy was simplified using

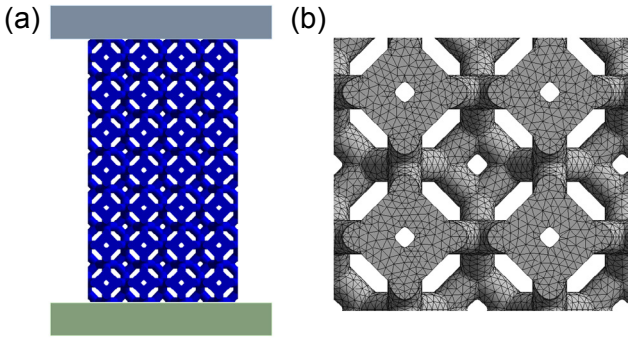


**Fig. 4: Finite element model of quasi-static compression (a) and its meshing (b)**

the bilinear isotropic strengthening model in the finite element analysis. The properties for the IN718 superalloy in the finite element simulation are shown in Table 2.

**Table 2: Properties of the matrix material (IN718) in finite element simulation**

| Elastic modulus $E$ (Pa) | Poisson's ratio $V$ | Yield strength $\sigma$ (MPa) | Tangent modulus $E_T$ (Pa) | Density $\rho$ (kg·m$^{-3}$) |
|---|---|---|---|---|
| 1.86×10$^{11}$ | 0.31 | 678 | 4.66×10$^{10}$ | 8,240 |

# 3 Results and discussion

## 3.1 Microstructure

Metallic lattice structures with porosities of 71%, 82%, 88%, and 92% were prepared. Figure 5 show the top-view SEM images of all the printed samples with different porosities. The manufacture of metallic lattice structures with different porosities was achieved by adjusting the $L/d$ ratio.

In the manufacturing process, production-related defects may occur, such as pores, cracks, and instance of incomplete molten metal adhering to the surface of product [34]. Through utilizing appropriate printing parameters, most of the internal pores and cracks are eliminated. However, many spherical particles remain on the surface, where they undergo melting and stick to the matrix, ultimately forming particles with neck-like characteristics, as shown in Fig. 5. These particles are attached to the surface due to the thermal effect of LPBF processing [11], and distributed across the surface in an extremely uneven manner. These particles may induce residual stress during cooling [35], which could act as the stress concentration points or crack sources. It has been pointed out that the presence of particles on the surface, as shown by the circle in Fig. 5, does not significantly affect the mechanical properties [36-37]. At the same time, the step effect caused by layer-by-layer printing can be seen in Fig. 5(a). This effect is minor for the overall structure.

The additive manufacturing process involves separating the three-dimensional model into sliced planes with different thicknesses and stacking them layer by layer through material accumulation. This process produces a noticeable ladder effect, and the resulting entities will exhibit certain shape errors compared to the model. Additionally, in the layer-by-layer stacking process, each layer will inevitably cause the adhesion of particles on the outermost layer, which will eventually affect the manufacturing accuracy of the surface shape. In the scanned image, both the ladder effect and the surface-adhered particles can be observed. The schematic diagram of the ladder effect and the particles adhered to the surface are shown in Figs. 5(e) and (f). The adhesion of these particles generally leads to positive deviation when compared with the designed geometric model, resulting in obvious irregularities. Fewer particles adhered to the plane ($XY$), but more adhered in the printing $Z$ direction, and this adhesion is closely related to the specific surface area. The smaller the porosity of the pattern, the greater number of particles attached in the printing direction.

The internal quality of the metallic lattice structures was examined using micro-CT. The micro-CT reconstruction slice morphology of the metallic lattice structures is shown in Fig. 6. By observing the different stages of $X$, $Y$, and $Z$ directions, it is found that the density is close to the theoretical density in all directions, and optimal densification is achieved without defects. Therefore, the prepared metallic lattice structures exhibit good internal forming quality in this work.

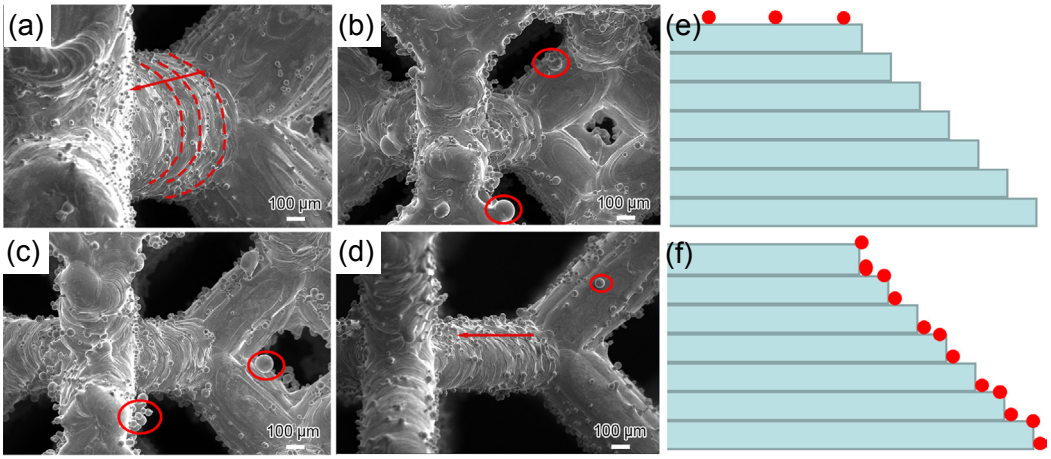


**Fig. 5: SEM images of Kelvin structure with different porosities: (a) 71%; (b) 82%; (c) 88%; (d) 92%, and schematic diagram of step effect and particles adhering to the surface (e)–(f)**

At the same time, the surface deviation of the metallic lattice structures was analyzed to evaluate the manufacturing accuracy. The micro-CT image provides the true shape of a component in the additive manufacturing process. By comparing it with the original design dimensions, it can be concluded that certain areas do not align with the design specifications. In the early stages of manufacturing, both positive and negative deviations are observed in the single layer in Figs. 6(a, d, g). As the number of printed layers increases, the strut displays similar characteristics in Figs. 6(b, e, h). Many positive deviations are seen between the struts, while negative deviations occur at or near the joints between struts in Figs. 6(c, f, i). Through the whole printing process, the maximum size deviation is approximately 0.05 mm, which is observable in the previous SEM micrograph in Fig. 5. There is a clear size deviation at the connection between strut, which aligns with the findings in the literature [12].

An IN718 Kelvin lattice structure with a porosity of 92% was fabricated, as shown in Fig. 7(a). After slicing layer by layer, the entire printed Kelvin structure was reconstructed. Through the reconstructed model, the printed surface can be intuitively

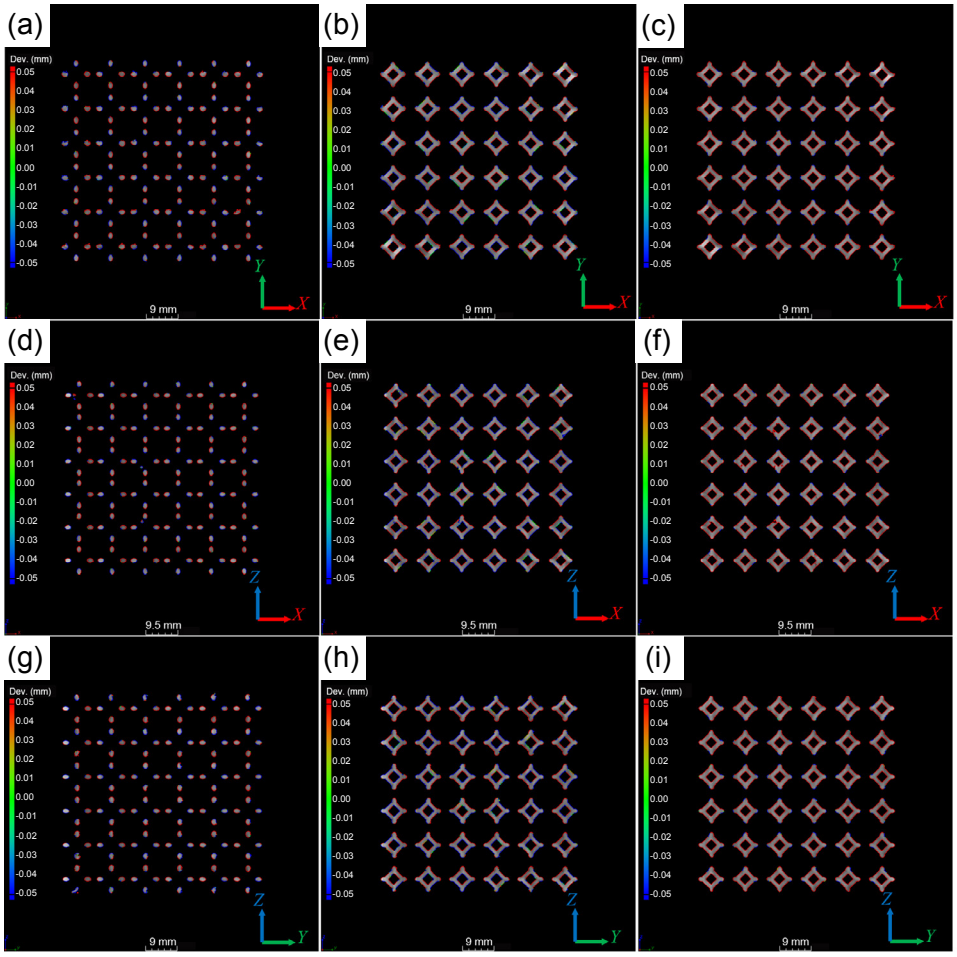


**Fig. 6: Surface deviation distribution in different directions of Kelvin lattice structures: (a)–(c) *XY*; (d)–(f) *ZX*; (g)–(i) *ZY***

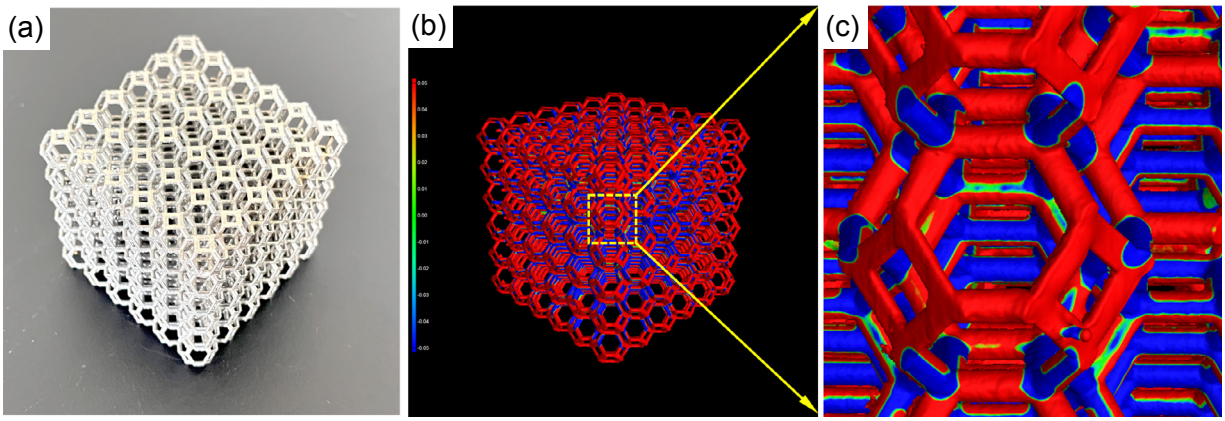


**Fig. 7: Manufactured Kelvin lattice structure with 92% porosity (a), 3D surface deviation diagram of micro-CT reconstructed model and original model (b), and local enlargement of (b) (c)**

observed, thereby aiding in the evaluation and improvement of surface manufacturing accuracy. The dimensional deviation between the reconstructed morphology and the designed lattice is shown in Fig. 7(b). The overall forming accuracy is high, with the overall deviation controlled at about 0.05 mm, mainly focusing on the edge and surface design. Figure 7(c) shows the dimensional deviation of a locally enlarged diagram. Its surface exhibits obvious positive and negative deviations, which are caused by the continuous heating and remelting of the molten pool.

## 3.2 Mechanical properties and finite element analysis

Based on the measured mechanical properties of the as-printed IN718 matrix material, the tensile curve for the printed tensile sample was obtained. As shown in Fig. 8, the yield strength of the IN718 matrix material is 678 MPa, and the elastic modulus is 186 GPa.

Figure 9 shows the simulated compression stress cloud diagram of the Kelvin lattice structures. The top and bottom plates were defined as rigid bodies. According to the simulation

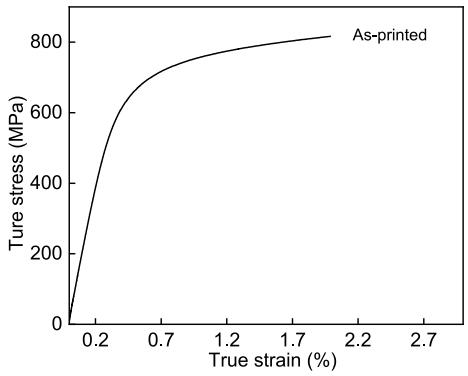


Fig. 8: True stress-strain curve of printed IN718 material

results of compression behavior, the deformation behavior can be divided into three distinct stages: the elastic deformation stage, plastic yielding stage, and the densification stage. At the same time, it can also be observed that the Kelvin lattice structures exhibit a uniform distribution of stress and deformation during the whole compression process.

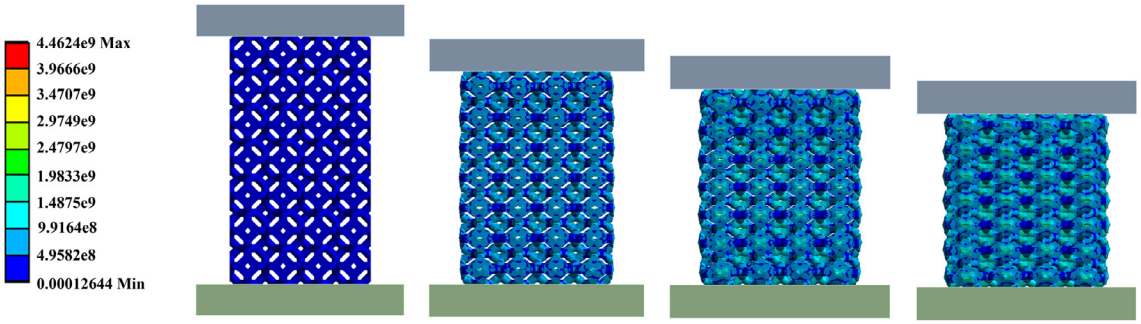


Fig. 9: Simulated compression stress cloud diagram of Kelvin lattice structures

According to the original design parameters, the theoretical porosity ($P$) of the designed model can be calculated using designing software (Unigraphics NX). The simulation results in Table 3 demonstrate the corresponding relationship between the $L/d$ ratio and porosity. The relationship curve between $L/d$ and porosity, drawn using MATLAB software, is given in Fig. 10.

Table 3: Relationship between *L/d* ratio and porosity of the Kelvin lattice structures

| *L/d* | *P* (%) | *L/d* | *P* (%) |
|---|---|---|---|
| 1 | 43 | 1.8 | 79 |
| 1.2 | 58 | 2 | 82 |
| 1.25 | 60 | 2.25 | 86 |
| 1.4 | 67 | 2.5 | 88 |
| 1.5 | 71 | 2.67 | 89 |
| 1.6 | 74 | 3 | 92 |
| 1.7 | 76 | 3.3 | 93 |
| 1.75 | 77 | 3.2 | – |

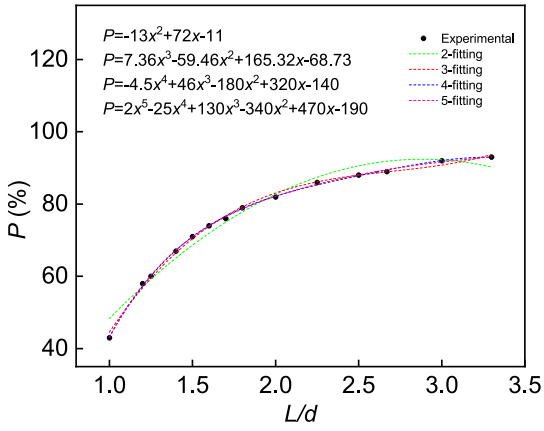


Fig. 10: Relationship between the *L/d* ratio and the porosity of the Kelvin lattice structures

With the increase of the order of the polynomial function, the residual value of the precision evaluation index decreases. In other words, the higher the polynomial order, the better the precision in Fig. 10. By comparing the fitting polynomial function with the real data point, it can be observed that the cubic polynomial exhibits a close correlation with the true values, and the trend of the curve is consistent with reality. Therefore, a cubic polynomial function was chosen to fit the

curve. The fitting relationship between the porosity and the aspect ratio ($L/d$) is shown in Eq. (4):

$$P = 7.36(\frac{L}{d})^3 - 59.46(\frac{L}{d})^2 + 165.32(\frac{L}{d}) - 68.73 \quad (4)$$

After establishing the relationship between the aspect ratio and porosity of metallic lattice structures, porosity is used to control the performance of metallic lattice structures. In the design of metallic lattice structures, the following equations are generally used to link performance and porosity [38-39], which were established by Gibson and Ashby when studying the quasi-static compressive properties of porous materials [27,40-41].

$$\frac{X^*}{X} = \alpha\left(\frac{\rho^*}{\rho}\right)^n \quad (5)$$

$$\frac{X^*}{X} = \alpha\{1-P\}^n \quad (6)$$

where $X^*$ represents the properties of metallic lattice structures, $X$ represents the properties of the matrix material, $\rho^*$ represents the density of metallic lattice structures, $\rho$ represents the density of the matrix material, $P$ represents the porosity of metallic lattice structures, $\alpha$ is a performance constant, and $n$ is the fixation index.

Therefore, the static properties of metallic lattice structures are determined by establishing the relationship between the equivalent elastic modulus and yield strength of the metallic lattice structures and porosity. Generally, metallic lattice structures follow a three-stage pattern during quasi-static compression: a linear elastic stage, a plastic platform stage, and a densification stage [42].

However, the traditional Gibson and Ashby model is not specifically tailored for the additively manufactured metallic lattice structures, and its predicted value often deviates significantly from actual messurement. To improve accuracy, the established values of porosity and $L/d$ ratio of the strut are incorporated into the classical Gibson and Ashby model and subsequently fitted and adjusted. The revised Gibson-Ashby model is as follows:

$$\frac{X^*}{X} = \alpha\left(\frac{\rho^*}{\rho}\right)^n\left(\frac{L}{d}\right)^m \quad (7)$$

Thus, the stress-strain curves of Kelvin lattice structure with different porosities were obtained through quasi-static compression finite element simulation. From these stress-strain curves, a relationship among porosity, equivalent elastic modulus, and yield strength of Kelvin lattice structure was established. The equivalent elastic modulus and yield strength of Kelvin lattice structures with different porosities are shown in Table 4. According to the finite element numerical simulation results, a quadratic polynomial function was used to revise the Eq. (7), and the fitted curve is shown in Fig. 11.

Equation (8) shows the relationship between the equivalent elastic modulus ($E^*$) and the porosity of the Kelvin lattice structures:

$$\frac{E^*}{E} = 0.8273(1-P)^2 - 0.0023(1-P) - 0.0012 \quad (8)$$

Similarly, the equivalent yield strength of the Kelvin lattice structures with different porosities was also investigated through finite element numerical simulation. Figure 11(b) shows the fitting curve between the equivalent yield strength and porosity of the Kelvin lattice structures. The relationship between the equivalent yield strength ($\sigma^*$) and porosity of the Kelvin lattice structures was fitted by the quadratic polynomial. The fitted relation is shown in Eq. (9):

$$\frac{\sigma^*}{\sigma} = 0.87(1-P)^2 + 0.1106(1-P) + 0.0006 \quad (9)$$

**Table 4: Simulation values of equivalent elastic modulus and yield strength for the Kelvin lattice structures with different porosities**

| Porosity, $P$ (%) | Equivalent elastic modulus, $E^*$ (Pa) | Equivalent yield strength, $\sigma^*$ (MPa) |
|---|---|---|
| 71 | $12.55\times10^9$ | 71.63 |
| 76 | $8.74\times10^9$ | 52.07 |
| 82 | $4.46\times10^9$ | 34.35 |
| 88 | $2.11\times10^9$ | 16.15 |
| 92 | $0.68\times10^9$ | 10.97 |

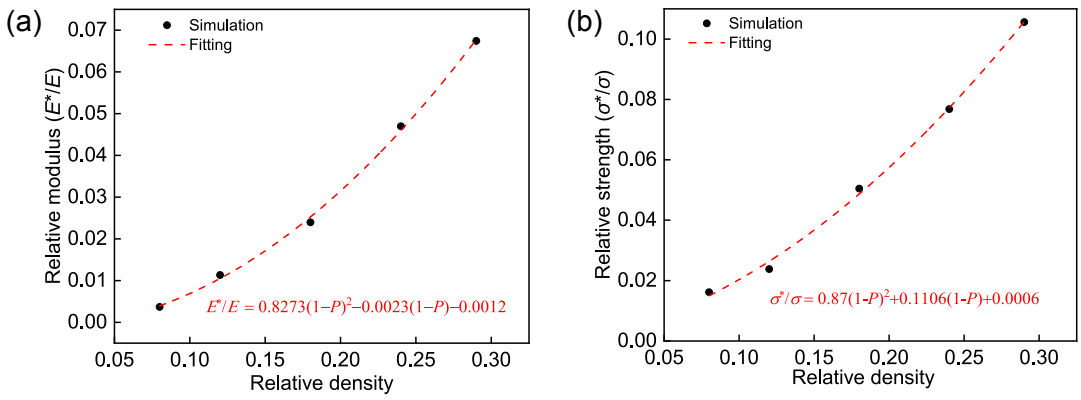


**Fig. 11: Fitting curves between the porosity and the elastic modulus and yield strength of the Kelvin lattice structures: (a) elastic modulus; (b) yield strength**

Figure 12 shows the performance predictions by different Gibson-Ashby models and compares them with our modified Gibson-Ashby model [5,10]. The results obtained from the modified model proposed in this study align well with the predictions of the classical Gibson-Ashby model. The relationship between porosity and mechanical properties is obtained with a fixed function, as shown in Eqs. (8) and (9), rather than a broad performance prediction. Simultaneously, a compression experiment of the Kelvin lattice structures was carried out [Fig. 12(c)], and the modified Gibson-Ashby model was validated. It is found that the modified Gibson-Ashby model demonstrates higher accuracy. Its superiority lies in the mathematical expression of the porosity of the design structure, allowing for accurate prediction of the mechanical properties through fitting. This method is universally applicable to other types and configurations of metallic lattice structures, and it can predict their mechanical properties based on the same principle.

### 3.3 Isotropy of lattice structure and energy absorption

In order to verify the isotropy of the Kelvin lattice structures, metallic lattice structures with a porosity of 92% were tested in the *X* and *Y* directions, perpendicular to the printing direction. The compression curves are shown in Fig. 13. The sample size was 40 mm×40 mm×40 mm. The stress-strain curves of the *X*, *Y* directions and *Z*-direction [which represents compression in the printing direction, as shown in Fig. 13(c)] demonstrate similar mechanical properties. The stress values in the three directions remain between 15–16 MPa, and the deformation is generally consistent. However, during the compression

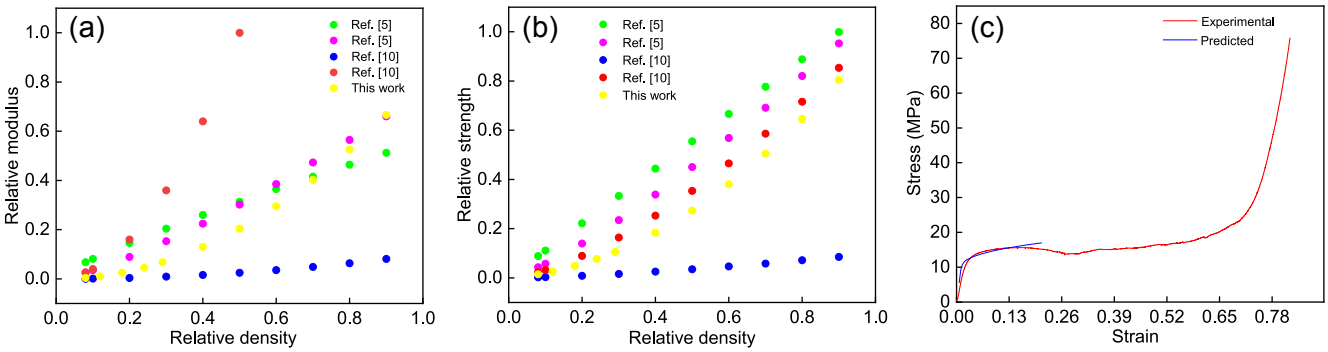


**Fig. 12: Comparison of normalized elastic modulus obtained from the modified Gibson-Ashby model and experiments: (a) relative modulus; (b) relative strength; (c) experimental verification**

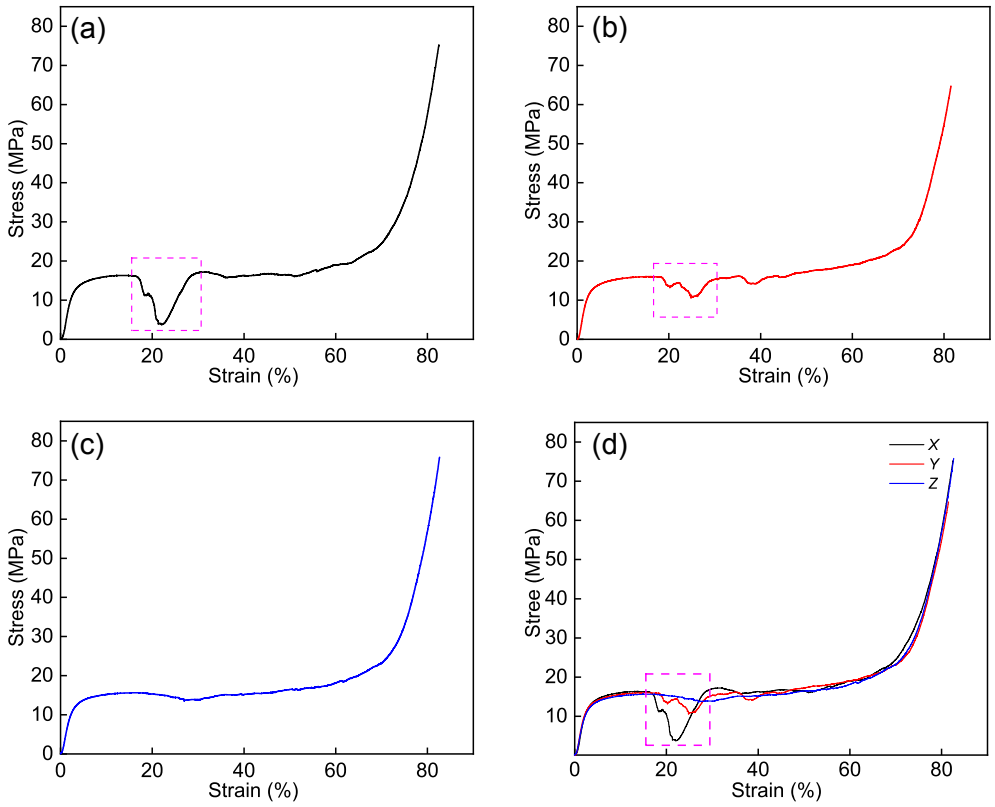


**Fig. 13: *X*-direction compression curve (a), *Y*-direction compression curve (b), *Z*-direction compression curve (c), and comparison of compression curves in three directions (d)**

process, there is an obvious stress decrease at the marked area in Figs. 13(a, b), which may be due to significant printing defects in the compression direction. The defect exists only at specific positions, and the stress-strain curve shows a relatively smooth trend as compression progresses. The stress platforms in the three directions are almost identical in Fig. 13(d). From the above experimental results, it can be concluded that the Kelvin lattice structures exhibit nearly isotropic mechanical properties in the *X*, *Y*, and *Z* directions.

This characteristic primarily arises from the inherent features of the Kelvin structure, where all the three directions have symmetric structural characteristics, thus allowing the prepared lattice structure to exhibit isotropy. At the same time, the printed IN718 lattice structures demonstrate good compression performance, as they do not fracture even when compressed to a large deformation, with maximum deformation reaching approximately 80%, as shown in Figs. 12(c) and 13. The compression curve can be divided into three distinct stages: the elastic zone, the platform zone, and the densification zone. It exhibits the same compression characteristics as most metal foams [43-45].

Additionally, the energy absorption characteristics of the lattice structures were studied. The energy absorption performance of the lattice structures was evaluated based on their energy absorption capacity per unit volume. The calculation equation of energy absorption $C$ in the interval $[\varepsilon_1, \varepsilon_2]$ is as follows [42]:

$$C = \int_{\varepsilon_1}^{\varepsilon_2} \sigma_m d\varepsilon \tag{10}$$

where $\sigma_m$ is stress, $\varepsilon$ is strain.

The energy absorption of the lattice structure corresponds to the area under the stress-strain curve. As illustrated in Fig. 14, this value progressively increases during compression, reaching 16.23 MJ·m$^{-3}$, 15.48 MJ·m$^{-3}$, and 16.24 MJ·m$^{-3}$ along the *X*, *Y*, and *Z* directions, respectively.

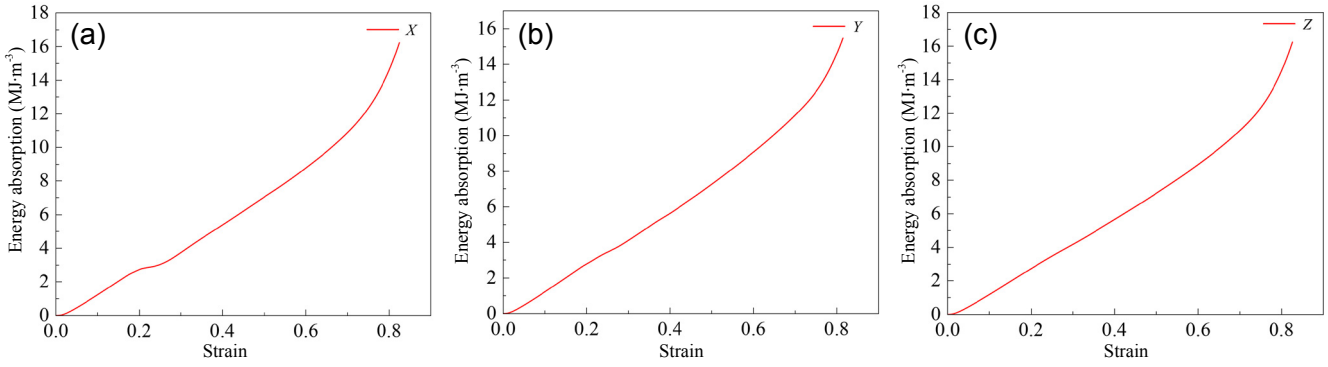


**Fig. 14: Energy absorption curve: (a) *X*-direction; (b) *Y*-direction; (c) *Z*-direction**

During the platform zone, the metallic lattice structures are supported by both the matrix materials and the designed structures to achieve energy absorption. The designed platform stage should surpass practical application requirements. Within this strain range of platform, the structure maintains a consistent load-bearing capacity, while exhibiting enhanced impact resistance. The strain at the end of the platform zone is approximately 70%, after which the material begins to densify. At the third stage, the energy absorption value of the material matrix increases. The lattice structure in this stage is completely destroyed.

## 4 Conclusions

In summary, this study employed laser powder bed fusion to fabricate strut-based Kelvin lattice structure specimens, investigating their mechanical performance and manufacturing quality. The following conclusions are achieved:

(1) A quantitative predictive model between porosity and mechanical properties of Kelvin lattice structures was established through combined numerical simulation and experimental validation. This research method has universal adaptability to other metallic lattice structures.

(2) Kelvin lattice structures exhibit smooth stress-strain responses with distinct yield plateaus, demonstrating spatial isotropy across three orthogonal axes. This mechanical uniformity enhances adaptability to complex loading scenarios while expanding potential engineering applications.

(3) Micro-CT characterization has demonstrated that by optimizing laser powder bed fusion parameters, manufacturing defects such as unmelted powders and internal voids can be effectively eliminated. This results in a dimensional accuracy of less than 0.05 mm. Furthermore, bidirectional dimensional tolerances, which are quantified through a 3D model-to-CT reconstruction analysis, confirm the unique capability of this methodology for non-destructive evaluation of metallic lattice structures. This technique allows for a detailed and accurate assessment of the structural integrity and dimensional accuracy of the lattice structures without causing any damage to the material.

## Acknowledgments

This work was financially supported by the Liaoning Province Applied Fundamental Research Program (No. 2023JH2/101700039) and Liaoning Province Natural Science Foundation (No. 2023-MSLH-328).

## Conflict of interest

The authors declare that they have no known competing financial interests or personal relationships that could have appeared to influence the work reported in this paper.

## References

[1] Al-Ketan O, Rowshan R, Abu Al-Rub R K. Topology-mechanical property relationship of 3D printed strut, skeletal, and sheet based periodic metallic cellular materials. Additive Manufacturing, 2018, 19: 167–183.
[2] Xiao Z, Yang Y, Xiao R, et al. Evaluation of topology-optimized lattice structures manufactured via selective laser melting. Materials & Design, 2018, 143: 27–37.
[3] Maskery I, Aboulkhair N T, Aremu A O, et al. A mechanical property evaluation of graded density Al-Si10-Mg lattice structures manufactured by selective laser melting. Materials Science and Engineering: A, 2016, 670: 264–274.
[4] Alsalla H, Hao L, Smith C. Fracture toughness and tensile strength of 316L stainless steel cellular lattice structures manufactured using the selective laser melting technique. Materials Science and Engineering: A, 2016, 669: 1–6.
[5] Wang P, Li X, Jiang Y, et al. Electron beam melted heterogeneously porous microlattices for metallic bone applications: Design and investigations of boundary and edge effects. Additive Manufacturing, 2020, 36: 101566.
[6] Carneiro V H, Rawson S D, Puga H, et al. Additive manufacturing assisted investment casting: A low-cost method to fabricate periodic metallic cellular lattices. Additive Manufacturing, 2020, 33: 101085.
[7] Wu B, Qiu Z, Dong B, et al. Effects of synchronized magnetic arc oscillation on microstructure, texture, grain boundary and mechanical properties of wire arc additively manufactured Ti6Al4V alloy. Additive Manufacturing, 2022, 54: 102723.
[8] Shah M R, Patel D, Pande S. Additive manufacturing integrated casting – A review. Materials Today: Proceedings, 2022, 62: 7199–7203.
[9] Nazir A, Gokcekaya O, Md Masum B K, et al. Multi-material additive manufacturing: A systematic review of design, properties, applications, challenges, and 3D printing of materials and cellular metamaterials. Materials & Design, 2023, 226: 111661.
[10] Maconachie T, Leary M, Lozanovski B, et al. SLM lattice structures: Properties, performance, applications and challenges. Materials & Design, 2019, 183: 108137.
[11] Sokollu B, Gulcan O, Konukseven E I. Mechanical properties comparison of strut-based and triply periodic minimal surface lattice structures produced by electron beam melting. Additive Manufacturing, 2022, 60: 103199.
[12] Seif M N, Richardson D J, Moody K M, et al. Stochastic approach for determining properties of randomly structured materials: Effects of network connectivity. Acta Materialia, 2022, 222: 117382.
[13] Korkmaz M E, Gupta M K, Robak G, et al. Development of lattice structure with selective laser melting process: A state of the art on properties, future trends and challenges. Journal of Manufacturing Processes, 2022, 81: 1040–1063.
[14] Kornievsky A, Nasedkin A. Numerical investigation of mechanical properties of foams modeled by regular Gibson-Ashby lattices with different internal structures. Materialia, 2022, 26: 101563.
[15] Park S Y, Kim K S, AlMangour B, et al. Effect of unit cell topology on the tensile loading responses of additive manufactured CoCrMo triply periodic minimal surface sheet lattices. Materials & Design, 2021, 206: 109778.
[16] Sos M, Meyer G, Durst K, et al. Microstructure and mechanical properties of additively manufactured AlSi10Mg lattice structures from single contour exposure. Materials & Design, 2023, 227: 111796.
[17] Alkhatib S E, Xu S, Lu G, et al. Rate-dependent behaviour of additively manufactured topology optimised lattice structures. Thin-Walled Structures, 2024, 198: 111710.
[18] Sun Q, Sun J, Guo K, Wang L. Compressive mechanical properties and energy absorption characteristics of SLM fabricated Ti6Al4V triply periodic minimal surface cellular structures. Mechanics of Materials, 2022, 166: 104241.
[19] Singh G, Pandey P M. Uniform and graded copper open cell ordered foams fabricated by rapid manufacturing: Surface morphology, mechanical properties and energy absorption capacity. Materials Science and Engineering: A, 2019, 761: 138035.
[20] Zhao W, He S, Wei X, et al. Quantitative relationships between cellular structure parameters and the elastic modulus of aluminum foam. Materials Science and Engineering: A, 2023, 868: 144713.
[21] Cheng H, Zhu X, Cheng X, et al. Mechanical metamaterials made of freestanding quasi-BCC nanolattices of gold and copper with ultra-high energy absorption capacity. Nature Communications, 2023, 14: 1243.
[22] Song B, Zhao X, Li S, et al. Differences in microstructure and properties between selective laser melting and traditional manufacturing for fabrication of metal parts: A review. Frontiers of Mechanical Engineering, 2015, 10: 111–125.
[23] Yang S, Han Q, Yin Y, et al. Effects of micrometer-sized $TiB_2$ on crack mitigation, mechanical and electrochemical performance of a Ni-based alloy fabricated by selective laser melting. Optics & Laser Technology, 2021, 142: 107240.
[24] Leung C L A, Marussi S, Atwood R C, et al. In situ X-ray imaging of defect and molten pool dynamics in laser additive manufacturing. Nature Communications, 2018, 9: 1355.
[25] Ghanavati R, Naffakh-Moosavy H, Moradi M, et al. Printability and microstructure of directed energy deposited SS316l-IN718 multi-material: Numerical modeling and experimental analysis. Scientific Reports, 2022, 12: 16600.
[26] Uhlířová T, Pabst W. Conductivity and Young's modulus of porous metamaterials based on Gibson-Ashby cells. Scripta Materialia, 2019, 159: 1–4.
[27] Banait S, Jin X, Campos M, et al. Precipitation-induced transition in the mechanical behavior of 3D printed Inconel 718 bcc lattices. Scripta Materialia, 2021, 203: 114075.
[28] Zhang X, Zhang K, Zhang B, et al. Additive manufacturing, quasi-static and dynamic compressive behaviours of ceramic lattice structures. Journal of the European Ceramic Society, 2022, 42: 7102–7112.
[29] Sir T W. On the division of space with minimum partitional area. Acta Mathematica, 1887, 11: 121–134.
[30] Kelvin W T, and Weaire D L. The Kelvin problem: Foam structures of minimal surface area. London: Taylor & Francis, 1996.
[31] Li X, Tan Y H, Wang P, et al. Metallic microlattice and epoxy interpenetrating phase composites: Experimental and simulation studies on superior mechanical properties and their mechanisms. Composites, Part A: Applied Science and Manufacturing, 2020, 135: 105934.
[32] Bonatti C, Mohr D. Mechanical performance of additively-manufactured anisotropic and isotropic smooth shell-lattice materials: Simulations & experiments. Journal of the Mechanics and Physics of Solids, 2019, 122: 1–26.
[33] Liu G, Su Y, Xin S, et al. Enhanced wear resistance of Ti reinforced Inconel 718 superalloy manufactured by laser directed energy deposition. Materials Characterization, 2024, 209: 113736.

[34] Liu G, Su Y, Pi X, et al. Achieving high strength 316L stainless steel by laser directed energy deposition-ultrasonic rolling hybrid process. Materials Science and Engineering: A, 2024, 903: 146665.
[35] Guo Y, Chen C, Wang Q, et al. Effect of porosity on mechanical properties of porous tantalum scaffolds produced by electron beam powder bed fusion. Transactions of Nonferrous Metals Society of China, 2022, 32: 2922–2934.
[36] Szymczyk P, Hoppe V, Ziółkowski G, et al. The effect of geometry on mechanical properties of Ti6Al4V ELI scaffolds manufactured using additive manufacturing technology. Archives of Civil and Mechanical Engineering, 2020, 20: 11.
[37] Choy S Y, Sun C N, Leong K F, et al. Compressive properties of Ti-6Al-4V lattice structures fabricated by selective laser melting: Design, orientation and density. Additive Manufacturing, 2017, 16: 213–224.
[38] Qi D, Yu H, Liu M, et al. Mechanical behaviors of SLM additive manufactured octet-truss and truncated-octahedron lattice structures with uniform and taper beams. International Journal of Mechanical Sciences, 2019, 163: 105091.
[39] Ruiz de G S, Jeffers J R T, Ghouse S. A validated finite element analysis procedure for porous structures. Materials & Design, 2020, 189: 108546.
[40] Ananda V, Saravana K G, Jayaganthan R, et al. Distortion prediction in Inconel-718 part fabricated through LPBF by using homogenized support properties from experiments and numerical simulation. Materials, 2022, 15.
[41] Alomar Z, Concli F. Compressive behavior assessment of a newly developed circular cell-based lattice structure. Materials & Design, 2021, 205: 109716.
[42] Wei Y, Li H, Han J, et al. Mechanical and damping performances of TPMS lattice metamaterials fabricated by laser powder bed fusion. China Foundry, 2024, 21(4): 327–333.
[43] Shi Q, Qin F, Li K, et al. Effect of hot isostatic pressing on the microstructure and mechanical properties of 17-4PH stainless steel parts fabricated by selective laser melting. Materials Science and Engineering: A, 2021, 810: 141035.
[44] Chen L Y, Liang S X, Liu Y, et al. Additive manufacturing of metallic lattice structures: Unconstrained design, accurate fabrication, fascinated performances, and challenges. Materials Science and Engineering: R, 2021, 146: 100648.
[45] Carraturo M, Alaimo G, Marconi S, et al. Experimental and numerical evaluation of mechanical properties of 3D-printed stainless steel 316L lattice structures. Journal of Materials Engineering and Performance, 2021, 30: 5247–5251.